MATERIALS SCIENCE

Emergent tetragonality in a fundamentally orthorhombic material

Anisha G. Singh[1,2,3]*, Maja D. Bachmann[1,2,3], Joshua J. Sanchez[4], Akshat Pandey[5], Aharon Kapitulnik[1,2,3,5], Jong Woo Kim[6], Philip J. Ryan[6], Steven A. Kivelson[1,2,5,7], Ian R. Fisher[1,2,3]

Symmetry plays a key role in determining the physical properties of materials. By Neumann's principle, the properties of a material remain invariant under the symmetry operations of the space group to which the material belongs. Continuous phase transitions are associated with a spontaneous reduction in symmetry. Less common are examples where proximity to a continuous phase transition leads to an increase in symmetry. We find signatures of an emergent tetragonal symmetry close to a charge density wave (CDW) bicritical point in a fundamentally orthorhombic material, $ErTe_3$, for which the two distinct CDW phase transitions are tuned via anisotropic strain. We first establish that tension along the *a* axis favors an abrupt rotation of the CDW wave vector from the *c* to *a* axis and infer the presence of a bicritical point where the two continuous phase transitions meet. We then observe a divergence of the nematic elastoresistivity approaching this putative bicritical point, indicating an emergent tetragonality in the critical behavior.

INTRODUCTION

The symmetry of a material prescribes much more than just the lattice vectors of a Bravais lattice. Tetragonal symmetry, for example, implies invariance of the crystal structure and hence crystal properties, under 90° rotations about the principle axis and certain other mirror and rotation symmetries depending on the space group. $ErTe_3$, like other rare-earth tritellurides (RTe_3), has a lower symmetry, belonging to the orthorhombic space group Cmcm (D_{2h}^{17}, no 63). The structure comprises bilayers of almost-square tellurium nets, which are separated along the *b* axis by RTe block layers. At room temperature, the *a* and *c* lattice parameters are almost equal, $a = 0.999c$, and moreover, it is possible to tune the material from $a > c$ to $a < c$ using externally applied anisotropic strain. However, despite the near equivalence of the in-plane lattice parameters, the presence of a glide plane between the tellurium bilayers (Fig. 1A) makes the material fundamentally orthorhombic. The glide plane is a nonsymmorphic symmetry element and cannot be removed by external strains. Thus, even when the material is strain-tuned to a point where the in-plane lattice parameters are exactly equal ($a = c$), the system does not have a fourfold rotational symmetry and hence can never be truly tetragonal. Nevertheless, as we find here, the presence of a strain-tuned charge density wave (CDW) bicritical point in $ErTe_3$, which occurs at a critical strain where $a \neq c$, yields signatures in the elastoresistivity of an emergent tetragonal symmetry associated with the critical fluctuations.

RTe_3 crystals host a unidirectional, incommensurate CDW. For unstrained $ErTe_3$, this onsets via a continuous phase transition at a critical temperature $T_{CDW} = 268$ K, with the wave vector oriented within the Te plane, along the *c* axis (*1*, *2*). The instability is driven, at least in large part, by a strongly *q*-dependent electron-phonon coupling. Softening of the associated phonon mode as $T \rightarrow T_{CDW}$ has been observed via inelastic x-ray scattering (*3*, *4*). The structural motifs that make up the building blocks of RTe_3 result in a near equivalence of the electronic structure and phonon spectrum in the two in-plane directions. This near equivalence is reflected in a simultaneous, but incomplete, softening of the phonon mode at a wave vector equal in magnitude to the CDW wave vector but oriented in the transverse (*a*-axis) in-plane direction. Previous calculations indicate that unidirectional order is favored for sufficiently strong electron-phonon coupling, even on a truly square lattice (*5*). Consequently, the inequivalence of the *a* and *c* axes in $ErTe_3$ has generally been thought to act as a weak symmetry breaking field, favoring the *c*-axis CDW state over the competing *a*-axis state.

The presence of CDW fluctuations along both the *a*- and *c*-axis directions (*3*), as well as the subsequent *a*-axis transition in $ErTe_3$ at a lower temperature (*6*), suggests that it is possible to tune between these two CDW states using anisotropic strain. The CDW order parameters ϕ_a and ϕ_c couple to normal strains (ϵ_{xx}, ϵ_{yy}, and ϵ_{zz}) as $\lambda_i^{jj}\epsilon_{jj}|\phi_i|^2$ where λ_i^{jj} are coupling constants. There are two immediate consequences of this: First, the material develops a spontaneous anisotropic strain when cooled through the CDW transition (i.e., a nonzero value of ϕ_c or ϕ_a will result in a nonzero value of ϵ_{xx}, ϵ_{yy}, and ϵ_{zz}). This is indeed observed: The lattice grows longer in the CDW wave vector direction and shorter in the transverse direction (*6*). Second, T_{CDW} can be tuned by strain (*7*).

No symmetry operations of the point group relate the various coefficients λ_i^{jj}. However, the near equivalence of the electronic and phonon structures in the two directions suggests that certain coefficients might be closely related. For example, it is not unreasonable to anticipate that $\lambda_c^{xx} \sim \lambda_a^{yy} \sim -\lambda_a^{xx}$ etc. If this is indeed the case, then relatively small strains would not only be able to tune T_{CDW} but also rotate the direction of the primary CDW wave vector from along the *c* axis to along the *a* axis. Previous elastoresistance and elastocaloric effect measurements point toward this possibility, although direct evidence has thus far been lacking (*7*).

It is important to note that while both ϕ_a and ϕ_c are superficially similar CDW states, they are in fact fundamentally distinct from a symmetry perspective, precisely because the crystal structure is

[1]Geballe Laboratory for Advanced Materials, Stanford University, Stanford, CA, USA. [2]Stanford Institute for Materials and Energy Sciences, SLAC, Menlo Park, CA, USA. [3]Department of Applied Physics, Stanford University, Stanford, CA, USA. [4]Department of Physics, Massachusetts Institute of Technology, Cambridge, MA, USA. [5]Department of Physics, Stanford University, Stanford, CA, USA. [6]Advanced Photon Source, Argonne National Lab, Lemont, IL, USA. [7]Rudolf Peierls Centre for Theoretical Physics, University of Oxford, Oxford, UK.
*Corresponding author. Email: agsingh@stanford.edu

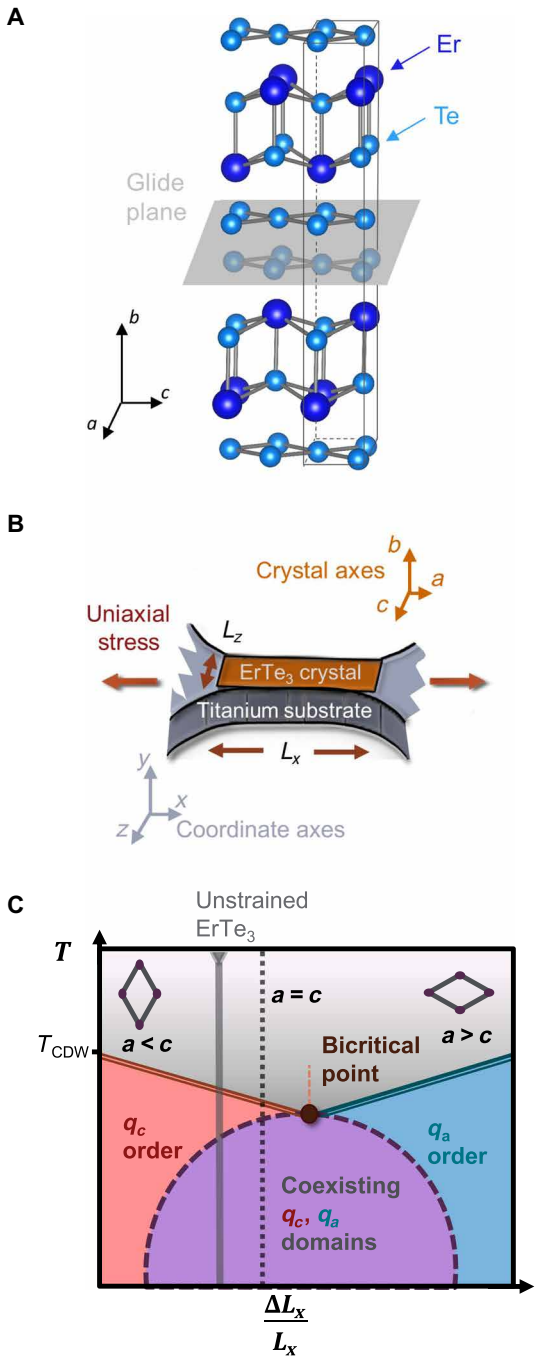

Fig. 1. Overview of uniaxial strain measurements of $ErTe_3$. (**A**) Crystal structure of $ErTe_3$, which comprises Te bilayers separated by ErTe blocks. Note that in the Cmcm space group setting, the in-plane lattice parameters are *a* and *c*, while the long *b* axis is perpendicular to the Te planes. A glide plane between the Te bilayers (illustrated) makes the material fundamentally orthorhombic. (**B**) Schematic diagram illustrating the neck of the titanium bowtie platform used for applying strain to a thin single crystal of $ErTe_3$ which is bonded to its surface. Insets indicate coordinate axes for the experiment (*xyz*) and the crystal axes of the sample (*abc*). Labels indicate the effective length L_x and width L_z of the platform. (**C**) Schematic diagram illustrating the proposed phase diagram of $ErTe_3$ as a function of $\Delta L_x/L_x$. Double solid lines represent continuous phase transitions, while dashed lines indicate first-order phase transitions. Insets indicate deformation of the Te lattice as a result of the strain. The putative bicritical point is labeled.

different in these two directions. At a minimum, this means that it is not given that strain should necessarily be able to rotate the CDW direction, and this must be verified experimentally. This is demonstrated here by performing high-resolution x-ray diffraction (XRD) experiments on samples held under continuously variable strain conditions. As shown schematically in Fig. 1C, the strain-tuned phase boundaries of the two distinct CDW states meet, within experimental uncertainty, at a bicritical point below which there is a first-order transition between the two ordered states. Because the experiment is conducted at fixed strain, not stress, the first-order transition results in a region of two-phase coexistence—i.e., domains of the two distinct CDW states—for intermediate values of the macroscopic strain $\Delta L_x/L_x$ and below the bicritical temperature. Noting that there are no symmetry-imposed reasons dictating the existence of such a multicritical point, it is intriguing to find signatures in elastoresistivity measurements of an emergent tetragonal symmetry near the strain-tuned bicritical point. Specifically, we observe the divergence of the nematic elastoresistivity approaching the bicritical point, although the material is structurally orthorhombic at this (and all) values of the applied strain. Such a divergence is ordinarily associated with the presence of nematic fluctuations in a tetragonal material. Hence, this suggests that the critical degrees of freedom in $ErTe_3$ acquire an emergent additional symmetry near the bicritical point. We discuss the origin of this effect using a simple mean field perspective.

RESULTS

High-resolution XRD

Using high-resolution XRD at a synchrotron light source, the evolution of CDW superlattice peaks with externally induced strain can be observed, providing a direct probe of the behavior of the CDW state. XRD measurements were completed at the Advanced Photon Source at Argonne National Lab at Sector 6-ID-B. Here, a sample environment has been developed to study samples with XRD with in situ strain tuning at cryogenic temperatures (*8*, *9*). A CS-130 Razorbill strain cell was used to apply variable strain to the samples (*10*). Data were taken at 11.2 keV. For $ErTe_3$, this corresponds to a penetration depth of roughly 50 μm, which is greater than the thickness of samples studied.

RTe_3 are very micaceous crystals. To maintain the crystallinity of the sample necessary for high-resolution XRD while strain-tuning, rather than mounting the sample directly into the Razorbill cell, the sample was affixed to a titanium "bowtie" platform designed for high strain transmission shown in Fig. 1B (*11*). The sample is less stiff than the Ti platform and therefore deforms together with the platform when a stress is applied. In our measurement configuration, the *a* axis was oriented in the stress direction (Fig. 1B), resulting in an anisotropic strain state, with ε_{xx} and ε_{zz} related by the Poisson ratio of the Ti platform.

The strain dependence of two CDW superlattice peaks are shown in Fig. 2A, confirming that anisotropic strain indeed reorients the primary CDW wave vector. In the absence of strain, the superlattice peak is observed along the *L* direction consistent with *c*-axis CDW order. As tension is applied along the *a* axis, effectively reversing the anisotropy of the system, the *L*-axis peak is suppressed while the *H*-axis peak emerges, consistent with reorientation of the CDW wave vector by 90°. Notably, reflective of the fundamental inequivalence of the in-plane axes, additional measurements reveal

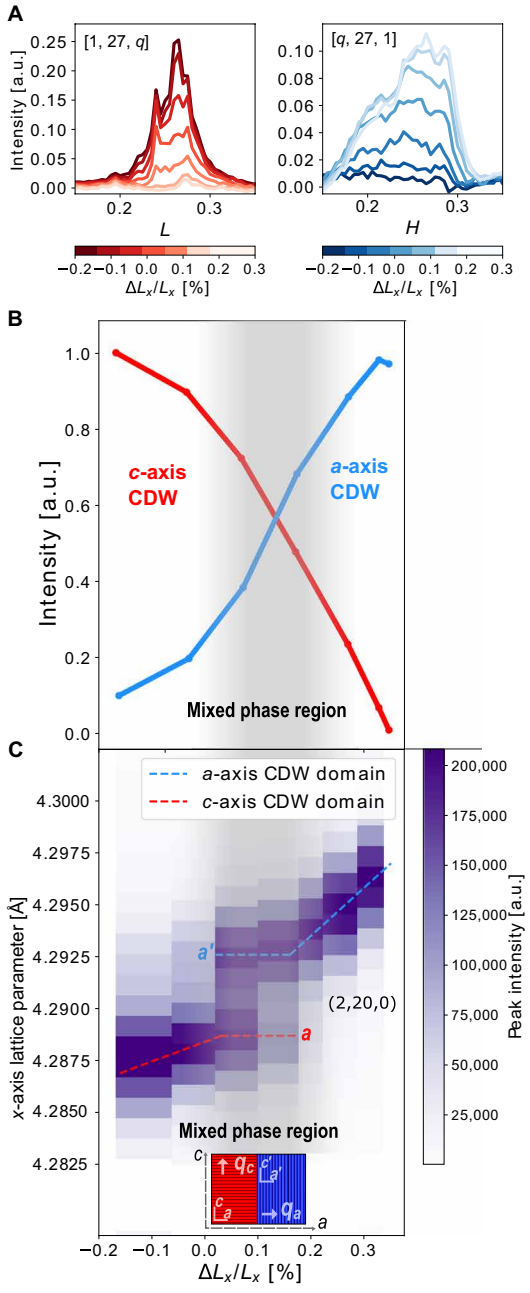

Fig. 2. XRD measurement of $ErTe_3$. (**A**) Observed superlattice peak intensities at (1, 27, q_{CDW}) and (q_{CDW}, 27, 1) at 200 K for different values of $\Delta L_x/L_x$. Under tension, the *c*-axis CDW peak is suppressed, while the *a*-axis CDW peak increases in intensity. Substantial broadening is observed in these structural peaks relative to free-standing crystals due to sample manipulation in the strain cell. (**B**) Integrated intensity of CDW superlattice peaks shown in (A) after background subtraction and normalization to adjacent Bragg peak intensities. Shaded region indicates mixed q_c, q_a phase. The mixed phase is defined here where neither CDW state exceeds 90% of the total CDW intensity. (**C**) Two-dimensional plot of the intensity of the (2,2,0) Bragg peak as a function of strain at 200 K. For intermediate strains, two peaks appear in the data due to the presence of domains, corresponding to regions of the material where the CDW wave vector is oriented along the *a* and *c* axes, respectively, as illustrated in the inset schematic. As consequence, the material effectively has two different lattice parameters along the *x* axis here labeled *a* and *a*′. In this strain range, the in-plane lattice parameters are constant since the system accommodates applied strain by changing the relative population of the two CDW domains. a.u., arbitrary units.

that the magnitude of the wave vector of the rotated CDW is close to but distinct from the unrotated value (see fig. S3). A similar rotation of the CDW wave vector with anisotropic strain was recently, independently observed for $TbTe_3$ (*12*). Our measurement also reveals a range of intermediate strains where the *c*- and *a*-axis CDW are simultaneously observed.

In Fig. 2B, the integrated intensity of both superlattice peaks is plotted as a function of $\Delta L_x/L_x$. The total CDW intensity is constant with strain but shifts between the *c*- and *a*-axis CDW states. In Fig. 2C, the behavior of a structural Bragg peak with an in-plane component is plotted for the same strain range, reported here as the lattice parameter along the *x* axis. Where the mixed CDW phase is observed, the Bragg peak splits, indicative of the emergence of domains. In this strain range, by rotating the CDW wave vector, the system adopts structural domains through which it can internally relax the applied stress. If, however, the applied strain exceeds the internal strain created by CDW rotation, a monodomain state is again achieved, and the lattice parameter varies monotonically with strain. Notably, the observation of such structural domains provides clear evidence that the simultaneous observation of q_a and q_c order is not the consequence of the emergence of a uniform homogeneous state comprising both wave vectors. Moreover, no peak was observed at the $q_a + q_c$ wave vector.

Elastoresistivity

Transport measurements can provide a useful window on electronic behavior close to phase transitions, with important information encoded in both its strain and temperature dependence. Here, we focus on the in-plane resistivity anisotropy ($\rho_a - \rho_c$), which is sensitive to the orientation of the CDW wave vector.

To perform accurate measurements of the in-plane resistive and elastoresistive anisotropies, a unique transport device was designed. The device incorporates a transverse measurement geometry which allows for direct determination of the resistive anisotropy in a single measurement [i.e., the measured voltage from the transverse contacts is directly proportional to $\rho_a - \rho_c$; see (*13*, *14*)]. Additional details of the device are presented in Fig. 3A and in the Supplementary Materials. The sample geometry was defined using a focused ion beam and uses the same titanium platform that was used for the XRD measurements as shown in Fig. 3B.

Measured values of the in-plane resistive anisotropy are plotted in Fig. 3C. For temperatures above the onset of CDW order, $T > T_{CDW}$, $\rho_a - \rho_c$ is close to but not exactly zero, consistent with the near equivalence of the two inequivalent crystallographic directions. Below the CDW transition, opening of the CDW gap results in an increase in the resistivity, although how this affects ρ_a and ρ_c depends on the orientation of the CDW wave vector. When the wave vector orients along the *c* axis, there is a larger change in ρ_a compared to ρ_c, resulting in a positive value of $\rho_a - \rho_c$ (*13*). This behavior has been previously understood using a simple Boltzmann transport approach including anisotropy in the Fermi velocity (*15*). Conversely, when the CDW orients along the *a* axis, the change in ρ_c is now larger than that of ρ_a resulting in a negative value of $\rho_a - \rho_c$ (*7*).

The resistivity data also reveal a change in T_{CDW} with strain. Taking the peak in the temperature derivative of the longitudinal resistivity $(\rho_a + \rho_c)/2$ as a measure of the critical temperature (see fig. S4), T_{CDW} can be determined as a function of strain and is shown in Fig. 4A. These data reveal a minimum value of T_{CDW} close to a critical value of $\Delta L_x/L_x \sim 0.13\%$. Since the data are plotted versus the

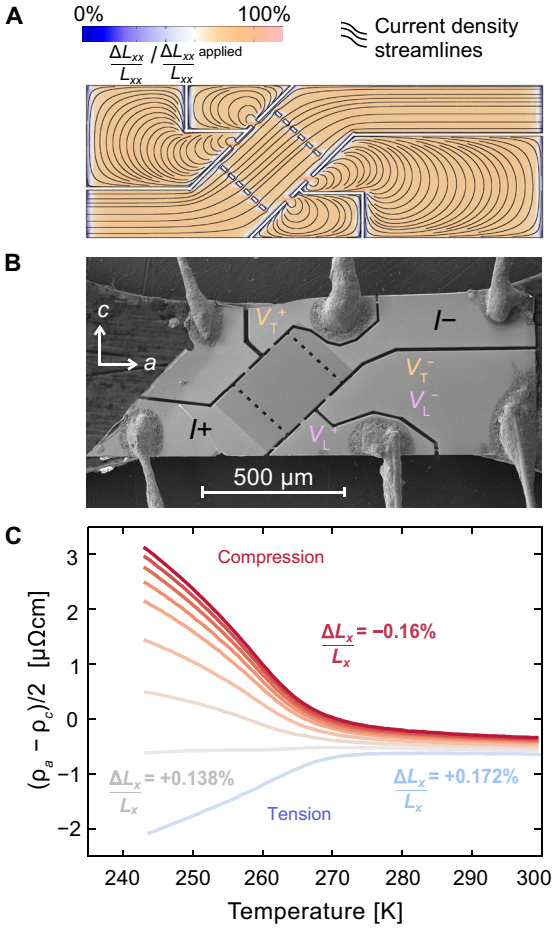

Fig. 3. Transport measurements in $ErTe_3$ under uniaxial strain. (**A**) Finite element simulations, using COMSOL Multiphysics, of the strain transmission and current flow for a typical transport device performed to establish optimal sample geometry to achieve large, homogeneous strain transmission as well as equipotentials that are closely parallel necessary for resistivity measurement. See the Supplementary Materials for additional details. (**B**) Scanning electron microscopy image of a typical device measured. Signal measured between the VT ± contacts, the transverse voltage, correspond to the in-plane resistive anisotropy ($\rho_a - \rho_c$)/2. (**C**) In-plane resistive anisotropy as a function of temperature for different (representative) values of compressive and tensile strain applied parallel to the *a* axis of the sample.

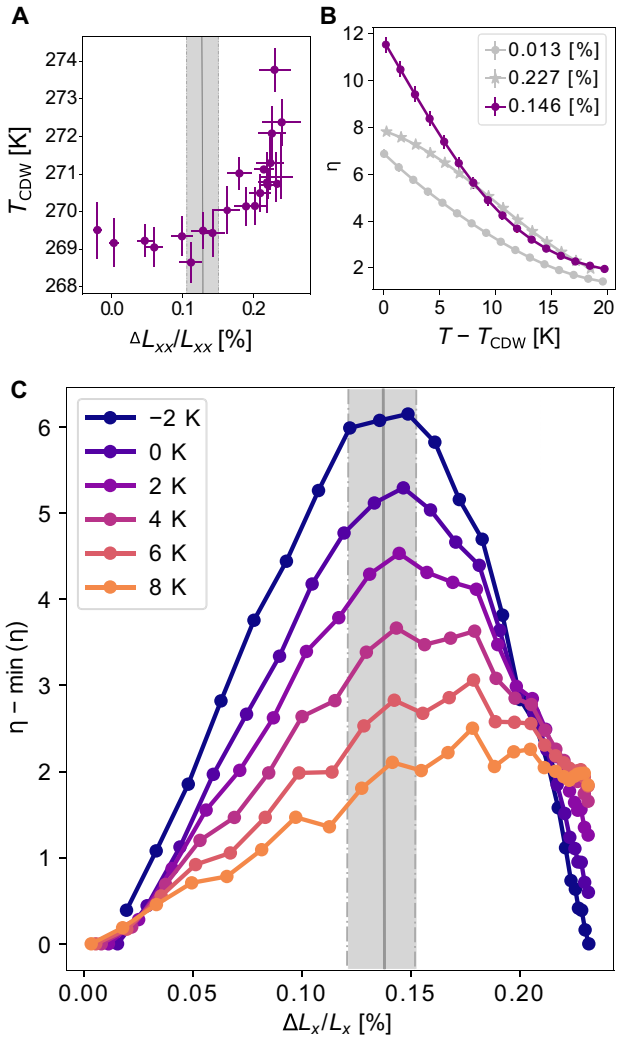

Fig. 4. Elastoresistivity measurements of $ErTe_3$. (**A**) The strain dependence of T_{CDW}, as determined from the peak in the temperature derivative of the longitudinal resistivity ($\rho_a + \rho_c$)/2 (see fig. S4) and expressed here as a function of $\Delta L_x/L_x$. Vertical band marks the critical strain at which the strain derivative of T_{CDW} changes sign and its uncertainty. (**B**) In-plane elastoresistivity anisotropy versus temperature for fixed offset strains (labeled in legend). For strain values close to the critical strain (purple curve), this quantity diverges as *T* approaches T_{CDW}. While the strains in this plot are reported as a constant, these data were taken for a fixed voltage applied to the piezoelectric stack. The strain label is therefore an average over the temperature sweep with an uncertainty of ±0.02%. For this reason, the strain at which a maximum response is observed in these temperature sweeps differs slightly from the maximum strain response reported in (C), where instead strain sweeps at constant temperature are reported. (**C**) In-plane elastoresistive anisotropy, η as defined in Discussion, versus strain for fixed relative temperature. The minimum value of η for a given relative temperature is subtracted from all data at that temperature to facilitate comparison across temperatures on a single plot. Vertical band marks the critical strain and its uncertainty.

macroscopic or applied strain rather than intrinsic sample strain as experienced by each unit cell in the material, this minimum observed in T_{CDW} is potentially broadened since the intrinsic sample strain changes minimally in this region of the plot due to domain formation. The overall shape of the resistivity curves does not change on tuning through this value of the strain, indicating that the phase transitions remain continuous. Notably, this is the same strain for which $\rho_a - \rho_c$ does not increase or decrease below T_{CDW} (Fig. 3C), implying that T_{CDW} at this strain value marks the putative bicritical point at which the onsets of ϕ_a and ϕ_c CDW order coincide. As discussed earlier, there is no symmetry relation between the *a*- and *c*-axis CDW states. Consequently, the strain derivative of the critical temperature of the two states is not compelled to be the same and is indeed found to be the case, i.e., T_{CDW} is not an even function about the critical strain in Fig. 4A.

Inspection of the data shown in Fig. 3C also reveals that the largest changes in resistivity with respect to strain occur when the resistive anisotropy is smallest. To further investigate this, elastoresistance measurements were performed as a function of strain and temperature close to T_{CDW}. Using an AC strain technique, in which a small AC strain is superimposed on an offset DC strain and the resulting

change in resistivity is measured using a demodulation technique (*16*), we can directly and sensitively measure the strain derivative of the resistive anisotropy. This value, normalized by the longitudinal resistivity, is plotted as a function of the relative temperature ($T - T_{CDW}$) in Fig. 4B, for strains below, at, and above the critical strain. To determine the relative temperature, T_{CDW} as a function of $\Delta L_x/L_x$ was found by fitting the data shown in Fig. 4A to a smooth polynomial. The elastoresistivity data shown in Fig. 4B clearly peak upon approaching T_{CDW} at the critical strain value (purple data) but have a smaller magnitude and roll over for all other values of applied strain (gray data).

The same elastoresistivity coefficient is plotted as a function of strain in Fig. 4C for different values of the relative temperature. This reveals a clear maximum centered around the critical strain 0.13%. This is a remarkably robust observation and is not sensitive to the exact functional form used for the strain dependence of T_{CDW} (see fig. S5).

DISCUSSION

The differential "nematic" elastoresistance

$$\eta = \frac{1}{(\rho_a + \rho_c)} \frac{\partial(\rho_a - \rho_c)}{\partial(\epsilon_{xx} - \epsilon_{zz})} \quad (1)$$

has no special meaning in an orthorhombic material. The three normal strains, ϵ_{xx}, ϵ_{yy}, and ϵ_{zz}, all belong to A_{1g} representations in an orthorhombic point group, such that each strain can separately affect each of the terms ρ_a, ρ_b, and ρ_c in the resistivity tensor. Consequently, while this quantity is allowed to vary with strain and temperature, there are no symmetry constraints that would dictate singular behavior for this combination of coefficients.

In contrast, for a tetragonal material with a two-component order parameter (ϕ_x and ϕ_y), this coefficient (rotating the coordinate axes so the *x* and *y* directions are related by a fourfold symmetry) has a specific physical meaning. Now, a nematic order parameter can be defined $N = <\phi_x^2> - <\phi_y^2>$, a quantity which, above the critical temperature, measures differences in the fluctuations of the two components of the order parameter. Since *N* couples linearly to antisymmetric strain $\epsilon_{B1g} = (\epsilon_{xx} - \epsilon_{yy})/2$, a nematic susceptibility for the same symmetry channel, $\chi_{B1g} = \frac{\partial N}{\partial \epsilon_{B1g}}$, can be defined. In this instance, as has been extensively discussed in the context of Fe-based superconductors (*17*–*19*), the resistive anisotropy is linearly proportional to *N* for small values of *N*, such that the nematic elastoresistivity coefficient η is proportional to χ_{B1g} (*18*). Therefore, a divergence in η in a tetragonal material is evidence of a diverging nematic susceptibility. Such behavior has been observed for a variety of materials for which multicomponent order parameters are relevant, including Fe-based superconductors and $BaNi_2As_2$ (*17*, *20*).

This behavior is not anticipated for $ErTe_3$ since ϕ_a and ϕ_c do not belong to a multicomponent order parameter and a "permanent" inequivalence of *x* and *z* directions means that *N* has a finite value for all temperatures and strains (barring accidental degeneracies). Such a system would not show any singular behavior in the elastoresistivity beyond standard Fisher-Langer–like anomalies at the strain-tuned phase transition (*21*). The sharp increase of η observed for $ErTe_3$ approaching the putative bicritical point is therefore anomalous and is highly suggestive of an emergent tetragonal symmetry proximate to this point in the temperature-strain plane.

We initially adopt a simple mean field model to provide insight into this remarkable observation. To quartic order in the two order parameters, and neglecting gradient terms and the elastic energy, the contribution to the free energy density from the CDW is given by

$$\begin{aligned}\Delta F = {} & r_a|\phi_a|^2 + u_a|\phi_a|^4 + r_c|\phi_c|^2 + u_c|\phi_c|^4 + g|\phi_a|^2|\phi_c|^2 \\ & + \lambda_a{}^{xx}\epsilon_{xx}|\phi_a|^2 + \lambda_a{}^{zz}\epsilon_{zz}|\phi_a|^2 + \lambda_c{}^{xx}\epsilon_{xx}|\phi_c|^2 + \lambda_c{}^{zz}\epsilon_{zz}|\phi_c|^2\end{aligned} \quad (2)$$

where $|\phi_a|$ and $|\phi_c|$ describe the amplitude of the two incommensurate CDW states. Here, to account for the fact that the competition between the phases is sufficiently strong to yield a bicritical point, we consider $g > 2\sqrt{u_a u_c}$. The strain coupling terms have been previously defined, and we neglect equivalent terms in ϵ_{yy} for simplicity. In the simplest possible phase diagram as a function of ϵ_{xx}, ϵ_{zz}, and temperature, the planes defining T_{CDW} for each phase meet along a line of bicritical points (*22*). The experiment has a fixed relation between ϵ_{xx} and ϵ_{zz} defined by the Poisson ratio of the Ti platform, and thus, we observe two lines which meet at a single bicritical point (Fig. 4A).

At the bicritical point, the coefficients of quadratic terms in the free energy, r_a and r_c, have both been tuned to zero. Neglecting for now the strain terms, a simple redefinition of the units of either of the CDW order parameters can lead to an equivalence of the quartic terms, such that exchange of ϕ_a and ϕ_c leaves the free energy unchanged (see the Supplementary Materials for full derivation). In other words, to quartic order in ϕ_a and ϕ_c, and neglecting other terms in the free energy, there is an emergent tetragonal symmetry associated with the critical degrees of freedom, which is inherited by all thermodynamic and transport properties sensitive to the critical fluctuations.

Even within this mean field picture, however, this is clearly only an approximate symmetry. Considering if the strain terms had a strict tetragonal symmetry (i.e., $\lambda^{xx}{}_c = \lambda^{zz}{}_a = -\lambda^{xx}{}_a$, etc.), then rotation of the *x* and *z* axes would leave the free energy invariant. However, allowing inequivalence of these terms, or including gradient terms or other higher-order terms, all lead to an inequivalence of the *a* and *c* crystal directions. Thus, the mean field anticipation is for an emergent approximate higher symmetry close to the strain-tuned bicritical point. To the level of precision of the present experiments, this mean field perspective is sufficient to account for the divergence of the nematic elastoresistivity coefficient η upon approaching the putative bicritical point. A thorough treatment of the fluctuations, which we develop in a separate article, reveals that under certain circumstances, this emergent symmetry is in fact asymptotically exact upon approach to criticality (*22*), although it is unlikely that experiments with the present control of strain homogeneity could distinguish the associated proposed scaling behavior from the mean field expectations.

In closing, we comment on some wider implications of our observations. First, having established that modest strains can rotate the direction of the CDW in $ErTe_3$, we note that domain formation is to be anticipated whenever a crystal of RTe_3 is held under conditions that fix the lateral dimensions (if the spontaneous strain that develops at T_{CDW} exceeds that which is caused by fixing the sample dimensions). In particular, one should anticipate domain formation whenever thin samples are bonded to a platform. Since this is a standard geometry for many experiments, consideration of domain formation should be included in interpretation of a variety of experimental

results. Earlier scanning tunneling microscopy results showing domain formation on the surface of $TbTe_3$ crystals might be related to this phenomenology (*23*).

Second, while the specific symmetry element that renders $ErTe_3$ orthorhombic for all values of externally induced strains is a glide plane, other structural motifs, for example the 1d chains in $YBa_2Cu_3O_{7-\delta}$, can play a similar role. The present observations provide proof of principle that similar phenomenology of emergent higher symmetries could, at least in principle, be found in such systems.

Last, we note that these observations fall within a wider context of materials for which non-symmetry-enforced degeneracies appear to play a crucial role in establishing emergent properties. Other examples include the possible multicomponent superconducting state in UTe_2, another fundamentally orthorhombic material for which degeneracy of two singlet representations has been proposed (*24*); possible multicomponent superconducting states in Fe-based superconductors (arising from "accidental" degeneracy of singlet s- and d-wave states in these tetragonal materials) (*25*, *26*); and proposals for other exotic nonsymmetry-enforced multicomponent superconducting states in Sr_2RuO_4 (*27*–*29*).

MATERIALS AND METHODS

Crystal growth and sample preparation

Single crystals of $ErTe_3$ were synthesized via a self-flux method as described in (*1*, *2*). Typical crystals had a surface area between 1 and 2 mm^2 and were 0.5-mm thick. Before mounting the sample for strain measurement, the crystal's in-plane axes must be distinguished to select the strain axis. This is accomplished via XRD by using the forbidden extinctions of the Cmcm space group. (0, *K*, *L*) peaks are permitted for even values of *K*, while (*H*, *K*, 0) peaks are only permitted if both *H* and *K* are even. Hence, by comparing amplitudes of the (0, 6, 1), an allowed reflection, with (1, 6, 0), its forbidden counterpart, the *a* and *c* axes can be distinguished. No intensity was observed at the forbidden reflection, within the resolution of our measurement, indicating that samples measured do not exhibit any stacking faults in which the *a* and *c* crystal axes are reversed.

Sample mounting for strain measurement

The sample itself must be sufficiently thin to mitigate strain relaxation over its height. Finite element simulations indicated that the strain over the height of the sample is approximately homogeneous for crystals less than 50-μm thick (fig. S1). RTe_3 crystals exfoliate easily due to weak van der Waals bonding between the tellurium sheets, making it straightforward to cleave samples to thin dimensions. Similarly, a thin and stiff glue layer is necessary to mitigate strain relaxation. For sample mounting, angstrom bond epoxy was used which yielded glue layers between 5- and 10-μm thick. Samples used for XRD measurement were between 10- and 20-μm thick, while samples used for transport measurements were between 1- and 10-μm thick. In this range of thicknesses, all samples behaved similarly with strain; however, thinner samples were found to have worse crystallinity and hence were avoided for XRD measurement.

Device details for transport measurement

To perform transport measurements, the titanium platform which was to be used for the experiments was initially heated to high temperatures for several hours to create an insulating oxide layer before sample bonding. To achieve high and homogeneous strain transmission in the transport device, the sample length along the strain direction should be maximized, resulting in the choice of a diamond shape for the active area rather than more traditional bar shaped sample geometry. For this wider sample, multiple current injection points must then be defined to facilitate homogeneous current flow in the sample. Design was optimized using finite element simulations.

Supplementary Materials

This PDF file includes:

Supplementary Text
Figs. S1 to S5

REFERENCES AND NOTES

1. N. Ru, I. R. Fisher, Thermodynamic and transport properties of YTe_3, $LaTe_3$, and $CeTe_3$. *Phys. Rev. B* **73**, 033101 (2006).
2. N. Ru, Charge denisty wave formation in rare-earth tritellurides, thesis, Leland Stanford Jr. University (2008).
3. M. Maschek, S. Rosenkranz, R. Heid, A. H. Said, P. Giraldo-Gallo, I. R. Fisher, F. Weber, Wave-vector-dependent electron-phonon coupling and the charge-density-wave transition in $TbTe_3$. *Phys. Rev. B* **91**, 235146 (2015).
4. M. Maschek, D. A. Zocco, S. Rosenkranz, R. Heid, A. H. Said, A. Alatas, P. Walmsley, I. R. Fisher, F. Weber, Competing soft phonon modes at the charge-density-wave transitions in $DyTe_3$. *Phys. Rev. B* **98**, 094304 (2018).
5. H. Yao, J. A. Robertson, E. A. Kim, S. A. Kivelson, Theory of stripes in quasi-two-dimensional rare-earth tellurides. *Phys. Rev. B* **74**, 245126 (2006).
6. N. Ru, C. L. Condron, G. Y. Margulis, K. Y. Shin, J. Laverock, S. B. Dugdale, M. F. Toney, I. R. Fisher, Effect of chemical pressure on the charge density wave transition in rare-earth tritellurides $R\mathbf{Te_3}$. *Phys. Rev. B* **77**, 035114 (2008).
7. J. A. W. Straquadine, M. S. Ikeda, I. R. Fisher, Evidence for realignment of the charge density wave state in $ErTe_3$ and $TmTe_3$ under uniaxial stress via elastocaloric and elastoresistivity measurements. *Phys. Rev. X* **12**, 021046 (2022).
8. J. J. Sanchez, P. Malinowski, J. Mutch, J. Liu, J.-W. Kim, P. J. Ryan, J.-H. Chu, The transport–structural correspondence across the nematic phase transition probed by elasto X-ray diffraction. *Nat. Mater.* **20**, 1519–1524 (2021).
9. P. Malinowski, Q. Jiang, J. Sanchez, Z. Liu, J. Mutch, P. Went, J. Liu, P. Ryan, J.-W. Kim, J.-H. Chu, Suppression of superconductivity by anisotropic strain near a nematic quantum critical point. *Nat. Phys.* **16**, 1189–1193 (2020).
10. C. W. Hicks, M. E. Barber, S. D. Edkins, D. O. Brodsky, A. P. Mackenzie, Piezoelectric-based apparatus for strain tuning. *Rev. Sci. Instrum.* **85**, 065003 (2014).
11. J. Park, J. M. Bartlett, H. M. L. Noad, A. L. Stern, M. E. Barber, Rigid platform for applying large tunable strains to mechanically delicate samples. *Rev. Sci. Instrum.* **91**, 083902 (2020).
12. A. Gallo-Frantz, A. A. Sinchenko, D. Ghoneim, L. Ortega, V. L. R. Jacques, D. Le Bolloc'h, P. Godard, P.-O. Renault, P. Grigoriev, A. Hadj-Azzem, P. Monceau, E. Bellec, Charge-Density-Waves Tuned by Crystal Symmetry. arXiv. (2023). https://arxiv.org/abs/2306.15712.
13. P. Walmsley, I. R. Fisher, Determination of the resistivity anisotropy of orthorhombic materials via transverse resistivity measurements. *Rev Sci Instrum* **88**, 043901 (2017).
14. M. C. Shapiro, A. T. Hristov, J. C. Palmstrom, J. H. Chu, I. R. Fisher, Measurement of the B_{1g} and B_{2g} components of the elastoresistivity tensor for tetragonal materials via transverse resistivity configurations. *Rev Sci Instrum* **87**, 063902 (2016).
15. P. M. A. Sinchenko, P. Grigoriev, P. Lejay, P. Monceau, Spontaneous breaking of isotropy observed in the electronic transport of rare-earth tritellurides. *Phys. Rev. Lett.* **112**, 036601 (2014).
16. A. T. Hristov, J. C. Palmstrom, J. A. W. Straquadine, T. A. Merz, H. Y. Hwang, I. R. Fisher, Measurement of elastoresistivity at finite frequency by amplitude demodulation. *Rev. Sci. Instrum.* **89**, 103901 (2018).
17. J.-H. Chu, H.-H. Kuo, J. G. Analytis, I. R. Fisher, Divergent nematic susceptibility in an iron arsenide superconductor. *Science* **337**, 710–712 (2012).
18. M. C. Shapiro, P. Hlobil, A. T. Hristov, A. V. Maharaj, I. R. Fisher, Symmetry constraints on the elastoresistivity tensor. *Phys. Rev. B* **92**, 235147 (2015).
19. H. H. Kuo, J. H. Chu, J. C. Palmstrom, S. A. Kivelson, I. R. Fisher, Ubiquitous signatures of nematic quantum criticality in optimally doped Fe-based superconductors. *Science* **352**, 958–962 (2016).
20. C. Eckberg, D. J. Campbell, T. Metz, J. Collini, H. Hadovanets, T. Drye, P. Zavalij, M. H. Christensen, R. M. Fernandes, S. Lee, P. Abbamonte, J. W. Lynn, J. Paglione, Sixfold enhancement of superconductivity in a tunable electronic nematic system. *Nat. Phys.* **16**, 346–350 (2020).

21. A. T. Hristov, M. S. Ikeda, J. C. Palmstrom, P. Walmsley, I. R. Fisher, Elastoresistive and elastocaloric anomalies at magnetic and electronic-nematic critical points. *Phys. Rev. B* **99**, 100101 (2019).
22. S. A. Kivelson, A. Pandey, A. G. Singh, A. Kapitulnik, I. R. Fisher, Emergent $\mathbb{Z}_2$ symmetry near a charge density wave multicritical point. *Phys. Rev. B* **108**, 205141 (2023).
23. L. Fu, A. M. Kraft, B. Sharma, M. Singh, P. Walmsley, I. R. Fisher, M. C. Boyer, Multiple charge density wave states at the surface of $TbTe_3$. *Phys. Rev. B* **94**, 205101 (2016).
24. I. M. Hayes, D. S. Wei, T. Metz, J. Zhang, Y. S. Eo, S. Ran, S. R. Saha, J. Collini, N. P. Butch, D. F. Agterberg, A. Kapitulnik, J. Paglione, Multicomponent superconducting order parameter in UTe_2. *Science* **373**, 797–801 (2021).
25. P. J. Hirschfeld, M. M. Korshunov, I. I. Mazin, Gap symmetry and structure of Fe-based superconductors. *Rep. Prog. Phys.* **74**, 124508 (2011).
26. V. Grinenko, R. Sarkar, K. Kihou, C. H. Lee, I. Morozov, S. Aswartham, B. Büchner, P. Chekhonin, W. Skrotzki, K. Nenkov, R. Hühne, K. Nielsch, S.-L. Drechsler, V. L. Vadimov, M. A. Silaev, P. A. Volkov, I. Eremin, H. Luetkens, H.-H. Klauss, Superconductivity with broken time-reversal symmetry inside a superconducting s-wave state. *Nat. Phys.* **16**, 789–794 (2020).
27. S. A. Kivelson, A. C. Yuan, B. Ramshaw, R. Thomale, A proposal for reconciling diverse experiments on the superconducting state in Sr_2RuO_4. *npj Quantum Materials* **5**, (2020).
28. J. Clepkens, A. W. Lindquist, X. Liu, H. Y. Kee, Higher angular momentum pairings in interorbital shadowed-triplet superconductors: Application to Sr_2RuO_4. *Phys. Rev. B* **104**, 104512 (2021).
29. A. Romer, P. Hirschfeld, B. M. Andersen, Superconducting state of Sr_2RuO_4 in the presence of longer-range coulomb interactions. *Phys. Rev. B* **104**, 064507 (2021).

Acknowledgments

Funding: This work was supported by Department of Energy, Office of Basic Energy Sciences DE-AC02-76SF00515 (A.G.S., A.P., M.D.B., A.K., S.A.K., and I.R.F.). Work at the Advanced Photon Source was supported by US Department of Energy (DOE), Office of Science, and Office of Basic Energy Sciences under contract no. DE-AC02-06CH11357 (J.W.K. and P.J.R.). A.G.S. was additionally supported by the National Science Foundation Graduate Research Fellowship Program under grant no. DGE-1656518 and the Department of Energy Office of Science Graduate Student Research (SCGSR) Program. M.D.B. was additionally supported by the Geballe Laboratory for Advanced Materials Postdoctoral Fellowship. J.J.S. was additionally supported by the National Science Foundation MPS-Ascend Postdoctoral Research Fellowship, award no. 2138167. S.A.K. was additionally supported by the Leverhulme Trust International Professorship grant no. LIP-202-014. **Author contributions:** Conceptualization: A.G.S., I.R.F., A.K., S.A.K., J.W.K., and P.J.R. Methodology: A.G.S., I.R.F., J.W.K., P.J.R., A.K., and J.J.S. Software: J.W.K. Validation: P.J.R., A.K., J.W.K., I.R.F., and A.G.S. Resources: M.D.B. and A.G.S. Funding acquisition: A.K. and I.R.F. Investigation: A.G.S., J.J.S., M.D.B., J.W.K., and P.J.R. Visualization: A.K., I.R.F., and A.G.S. Writing—original draft: A.G.S., S.A.K., and I.R.F. Formal analysis: A.P., P.J.R., J.W.K., and A.G.S. Project administration: I.R.F., A.K., and P.J.R. Supervision: I.R.F., S.A.K., and P.J.R. Writing—review and editing: A.G.S., I.R.F., S.A.K., and A.K. **Competing interests:** The authors declare that they have no competing interests. **Data and materials availability:** All data needed to evaluate the conclusions in the paper are present in the paper and/or the Supplementary Materials.

Submitted 15 August 2023
Accepted 17 April 2024
Published 23 May 2024
10.1126/sciadv.adk3321